





Flexible optical imaging band system for the assessment of arthritis in patients with systemic lupus erythematosus

YOUNGWAN KIM,^{1,2,*}  ALESSANDRO MARONE,²  WEI TANG,³
YEVGENIYA GARTSHTEYN,³ HYUN K. KIM,^{2,4} ANCA D. ASKANASE,³
IOANNIS KYMISSIS,¹ AND ANDREAS H. HIELSCHER^{2,5,6}

¹Columbia University, Department of Electrical Engineering, 500 W. 120th Street, New York, NY 10027, USA

²New York University, Department of Biomedical Engineering, Brooklyn, NY 11201, USA

³Columbia University Irving Medical Center, Department of Medicine-Rheumatology, 650 W. 168th Street, New York, NY 10032, USA

⁴Columbia University Irving Medical Center, Department of Radiology, 650 W. 168th Street, New York, NY 10032, USA

⁵Columbia University, Department of Biomedical Engineering, 500 W. 120th Street, New York, NY 10027, USA

⁶ahh4614@nyu.edu

*yk2561@columbia.edu

Abstract: We have developed a flexible optical imaging system (FOIS) to assess systemic lupus erythematosus (SLE) arthritis in the finger joints. While any part of the body can be affected, arthritis in the finger joints is one of the most common SLE manifestations. There is an unmet need for accurate, low-cost assessment of lupus arthritis that can be easily performed at every clinic visit. Current imaging methods are imprecise, expensive, and time consuming to allow for frequent monitoring. Our FOIS can be wrapped around joints, and multiple light sources and detectors gather reflected and transmitted light intensities. Using data from two SLE patients and two healthy volunteers, we demonstrate the potential of this FOIS for assessment of arthritis in SLE patients.

© 2021 Optical Society of America under the terms of the [OSA Open Access Publishing Agreement](#)

1. Introduction

Systemic lupus erythematosus (SLE), also commonly referred to as “lupus”, is a chronic autoimmune disease that affects about 270,000 Americans. Worldwide approximately 20–70 per 100,000 people have SLE [1,2]. Women of childbearing age are affected about nine times more often than men [3]. While genetic and environmental factors play a role in the development of lupus, the pathophysiology of SLE is not fully understood. There is no known cure for SLE. Arthritis/arthralgia is one of the most common symptoms of lupus. Patients with SLE arthritis face formidable challenges from chronic, disabling symptoms, and progressive organ damage. SLE arthritis is associated with the cardinal signs of inflammation: redness, swelling, warmth, pain, and loss of function [4]. The heterogeneity of SLE and the short-comings of disease activity quantitation tools, both global and organ-specific (including arthritis measures), contribute to the many failures of SLE clinical trials. There are only four FDA-approved therapies for lupus (hydroxychloroquine, NSAIDs, corticosteroids, and Benlysta). This lack of approved lupus medications means that lupus investigators must find more precise measures of lupus activity, including better objective measures of lupus arthritis. SLE arthritis is difficult to evaluate because of the sometimes-evanescent nature of the symptoms, the limitations of physical exams, and the inadequacy of available imaging systems. The American College of Rheumatology (ACR) suggest various classification criteria that, at this point, do not include any imaging methods

[5]. Ultrasound was found to be unreliable because of high operator dependency, while MRI is considered too costly for routine monitoring [6]. There is a clear unmet need for a simple measurement tool that can objectively assess and monitor arthritis in lupus patients for use in clinical care and research.

Optical imaging techniques have the potential to address this need. Over the last decade this technology has been optimized for use in brain imaging, breast cancer, and peripheral artery diseases [7–14]. In all these applications, near-infrared light in the wavelength range of 650 to 900 nm illuminates the tissues of interest and the transmitted and reflected light intensities are measured. From these measurements, maps that show the spatial distribution of various physiological parameters can be computed. This includes, for example, maps of oxy-, deoxy-, and total hemoglobin concentrations ($[HbO_2]$, $[Hb]$, and $[THb]$, respectively), as well as water content ($[H_2O]$), and the tissue's absorption coefficient (μ_a) and scattering coefficient (μ_s). Changes in optical properties as related to physiologic changes form the basis for the diagnostic and monitoring capabilities of this technology.

Studies have also shown the clinical utility of optical methods for diagnosing rheumatoid arthritis in finger joints [15–22]. A detailed review of work before 2010 is provided in Ref. [15], and includes early work by the groups of H. Jiang [23], G. Müller [24], A. Hielscher [25], and R. Weissleder [26]. Our team advanced the optical assessment of joint diseases, especially optical tomographic imaging methods for rheumatoid arthritis. For example, in 2011 we showed that frequency-domain measurement at 600 MHz improve the reconstruction results [16]. Furthermore, we demonstrated that employing computer aided diagnostic tools, such as self-organizing maps (SOMs), and support vector machines (SVMs), lead to better classification results [17,18]. Using this approach, we achieved sensitivities and specificities above 90% in detecting RA. These studies, however, were limited to 1 illumination wavelength and only scattering and absorption coefficients were reconstructed. In 2016 the Dehghani team was the first to develop a multiwavelength tomographic joint imaging system [19,20] which allowed for directly extracting physiological information, such as the total hemoglobin concentration. The Dehghani system was further refined, and a recently completed pilot study achieved an area under the receiver operator curve (ROC) of 0.888 for detecting inflammation [21]. Their team employed a normalized Fourier transformation method applied to optical images acquired from the dorsal side with illumination on the palmar side. Subsequently, deep neural network methods further improved the diagnostic accuracy compared to the widely applied support vector machine learning algorithms [22].

While all these reports show clinical utility in diagnosing RA, none of these studies evaluated SLE arthritis. Furthermore, all of these systems rely on relatively complex and expensive imaging systems that, in many cases, are bulky and non-portable. In an attempt to reduce cost and enhance portability, researchers have introduced and developed compact optical imaging and spectroscopy systems [27–36]. These systems employed relatively low cost and small-sized optoelectronic devices: laser diodes (LDs) or light emitting diodes (LEDs) for light illumination and silicon photodiodes or complementary metal-oxide-semiconductor (CMOS) sensor for light detection. For example, Zhu et al. [28] introduced the use of a compact CMOS detector in a wearable system for real-time fluorescence image-guided surgery; while Di Sieno et al. [32] presented the first miniaturized pulsed laser source for time-domain diffuse optics. Some other groups developed portable systems including both miniaturized light sources and detectors [27,29,34–36]. These systems had a relatively rigid substrate for the electronics, leading to poor wearability. Probes designed with more flexible base materials [30,31,33] have the potential to be fully wearable. However, because of the limited number of illuminators and photodetectors and lack of geometrical consideration for illuminators and detectors restricted their studies to spectroscopic analysis and did not provide data adequate for tomographic reconstructions. Most importantly

though, none of these systems have been used for imaging arthritis and focused instead on brain [29,34] and breast imaging [31], as well as general tissue oximetry [27,30,33,35,36].

Here we present the development of a wearable flexible-electronic band system that can be wrapped around joints of the fingers and measure light transmission through the joints. A use of continuous wave illumination enables to assess the hemodynamic response to a venous occlusion generated by a 40 mmHg cuff inflation. In addition, this data can be used as input to an image reconstruction code that generates cross-sectional maps of the optical properties of joints. Using data from two lupus patients and two healthy volunteers, we provide the first clinical evidence to demonstrate the potential of this technology in the diagnosing SLE arthritis.

2. Method

2.1. Flexible system design

Our flexible optical imaging system (FOIS) consists of two key modules, a sensing band and a control band. The sensing band incorporates the light sources and detectors. The control band contains current controllers, signal amplifiers, and signal processors. Both bands are made of a polyimide (PI) film which is robust and thermally stable [37]. Furthermore, PI-films are very flexible allowing them to easily wrap around the finger joints [38].

The fabrication process of the imaging bands is illustrated in Fig. 1(a). First, electrodes made of ~ 15 μm -thick copper traces are patterned through a lithography process onto the polyimide substrate. The optoelectronic components are then placed onto these electrodes and soldered by means of the reflow process. Another polymer layer using parylene is deposited by chemical vapor deposition (CVD) to cover the exposed electrodes. This minimizes current leakage and reduces electrical noise. The total thickness of these patterned polymer substrates is below 100 μm . After designing the layout, the substrates were custom-fabricated by Best Technology, Ltd, to ensure durability and consistent performance in clinical measurements.

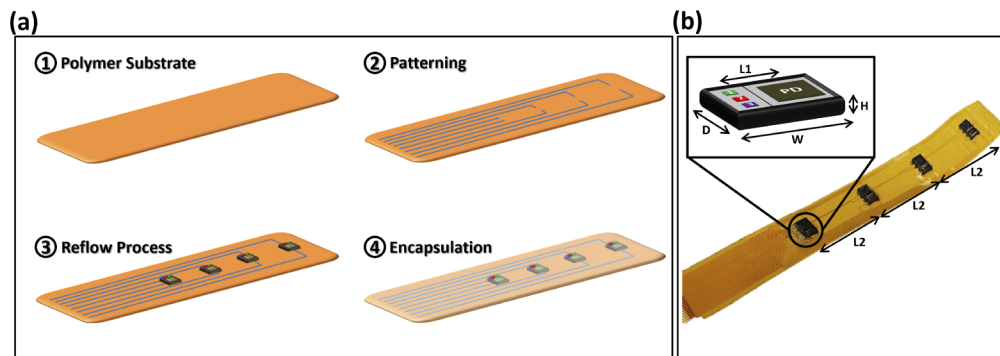


Fig. 1. Sensing band of FOIS. (a) Stepwise fabrication process for sensing bands. (b) Pictures of finished sensing band, possessing four pairs of integrated optoelectronic components (4.7 (W) \times 2.5 (D) \times 0.9 (H) in mm). Each integrated optoelectronic component consists of three light emitting diodes and one silicon-photodiode (Si-PD). The distance between LEDs and PD in these components is 3 mm (L1). The distance between components is 15 mm (L2).

The 10×80 mm band includes four integrated optical components [SFH7050, OSRAM – see Fig. 1(b)] that are used for light delivery and light detection. Each component includes three light emitting diodes (LEDs) at three different wavelengths ($\lambda = 530$ nm, 655 nm, and 940 nm) and one silicon photodiode (Si-PD), which has a sensitive area of 1.7 mm^2 . The components are positioned with a distance of 15 mm between them. In this way, one light-detector pair is approximately located on the top, bottom, and both sides of finger, respectively.

The control band used to operate the sensing band is shown in Fig. 2. It includes a current driver, a trans-impedance amplifier (TIA), a programmable gain amplifier (PGA), and an analog-digital converter (ADC). These are the minimum requirements to develop a simple, portable, low-cost system for reliable data acquisition. All electronic components are embedded in the same type of polyimide substrate as the one used for the sensing band. Therefore, the whole imaging system is flexible and wearable; it provides conformal attachment on any surface and an easy-to-use interface in human studies.

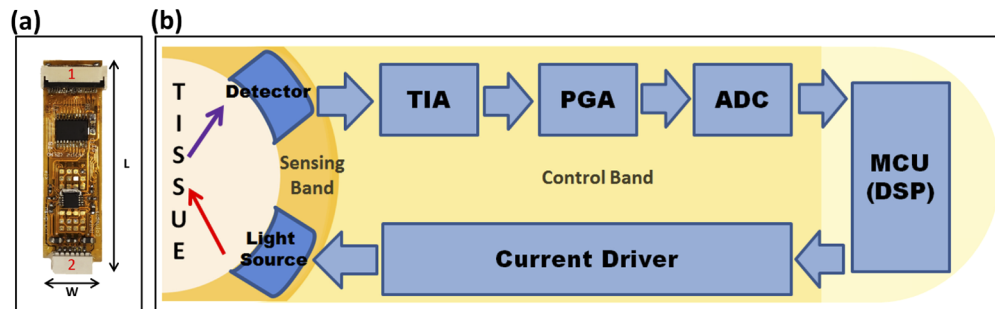


Fig. 2. Control band of FOIS. (a) Pictures of control band (10 mm (W) × 40 mm (L)) to access the sensing band connected to the pin 1. Pin 2 is connected to microcontroller. (b) Configuration for data acquisition (TIA: Trans-impedance amplifier, PGA: Programmable Gain Amplifier, ADC: Analog-Digital Converter, MCU: Microcontroller Unit, DSP: Digital Signal Processing).

The block diagram in Fig. 2(b) illustrates how data is acquired employing the sensing and control band. First, a driver (TLC59711, Texas Instrument) located on the control band provides a constant operating current for up to 12 light sources located on the sensing band. A well-controlled constant current is necessary to ensure a stable light intensity of the LEDs. Voltage controlled LEDs were not used because they tend to burn out frequently. Small variance of voltage or temperature change even at the same voltage, can lead to large current difference due to current-voltage characteristics of LEDs [39]. A microcontroller (ATmega328, Microchip), connected to the pin 2 [Fig. 2(a)], sets the current level for the light intensity of each LED at different wavelengths. The individual LEDs are turned on and off one at a time. With one LED turned on, all Si-PDs on the sensing band simultaneously detect diffusely transmitted and reflected light intensities and convert these into electric currents. This photocurrent is amplified and converted to a voltage signal by a TIA, located on the control band, with gain of 20,000. The voltage is further amplified by a PGA. An ADC (ADS1115, Texas Instrument) digitizes the amplified analog signals with 16-bit resolution and the microcontroller reads and transfers the digitized data to a computer through serial communication. All communications between integrated circuit components are based on I²C serial interface. All functions of the FOIS, such as optical power control, detector gain adjustment, and measurement time, are controlled by a LabVIEW-based graphic user interface (GUI).

The FOIS is a modular system that can be easily scaled. Therefore, multiple FOISs can be connected via I²C serial interface and operated as one system. Figure 3 shows a double imaging bands configuration between two FOISs that was used to gather data from the 4 volunteers in this study.

2.2. System characteristics

Figure 4 shows light intensity, current, and voltage characteristics of the LEDs that are part of the integrated optical component shown in Fig. 1(b). These properties were measured by a Keithley

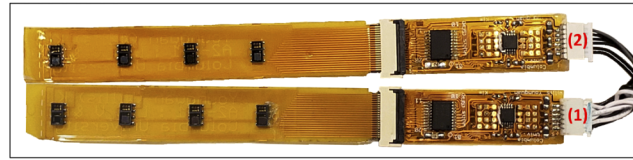


Fig. 3. Double bands configuration using two FOISs connected via serial interface between two connectors on the control bands (1) and (2).

2400 source-meter and a Thorlab PM100D power-meter. The maximum light intensity achievable are approximately 2.5 mW/cm^2 , 12 mW/cm^2 , and 15 mW/cm^2 , for the three wavelengths of 530 nm, 655 nm, and 940 nm, respectively. For our clinical study, the light intensities at all wavelengths were set to 2 mW/cm^2 with consideration for the maximum light intensity of 530 nm LED. The level of the current and voltage for 2 mW/cm^2 is displayed with an orange line in the figures. The dark current of the Si-PD is below 5 nA. The spectral sensitivities for each wavelength were determined to be 0.26 A/W (at 530 nm), 0.47 A/W (at 655 nm) and 0.77 A/W (at 940 nm), respectively.

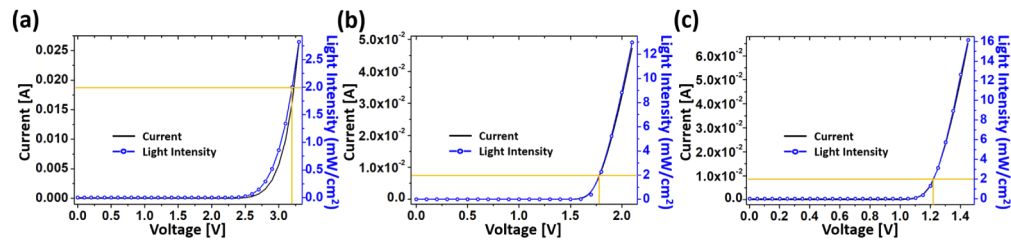


Fig. 4. Characteristics of LEDs. (a) 530 nm. (b) 655 nm. (c) 940 nm. Orange line indicates a forward voltage and current level for the light intensity of 2 mW/cm^2 .

Next, we investigated the stability of the LEDs and PDs within the whole system. Figure 5(a) shows the optical power (measured with a Thorlab PM100D power-meter) for consecutive trains of LED pulses consisting of three wavelengths of 530 nm, 655 nm, and 940 nm. For this test, the optical power at each wavelength was set to 2 mW/cm^2 . The fluctuation of the overall light emission was calculated in terms of relative standard deviation (RSD), which was 0.2%.

We also examined the stability of the Si-PD after the FOIS was attached to the finger. Figure 5(b) shows the stability under the given constant optical power at the wavelength of 940 nm. Stability data is shown in four and half minutes, which equals the length of the measurements performed during the clinical case studies (installation time: 0.5 ~ 1.5 minutes, data acquisition time: ~ 3 minutes). The overall signal fluctuation was observed to be about 2.0% yielding the SNR (signal to noise ratio) of 52 dB (In this work, SNR is defined as the ratio of mean value of the measured signals to the standard deviation of the measured signals for a period of baseline, which is a steady state when there is no external stimulus that can influence to the measured signals, $\text{SNR} [\text{dB}] = 10 \log_{10} \left| \frac{\text{Mean}(\text{signal})}{\text{std}(\text{signal})} \right|$.) The same test was performed at the other wavelengths and we found SNR values of 51 dB for 655 nm and 44 dB for 530nm. Overall, these tests demonstrate a fairly stable light emission and detectability within the system. At the given highest dark noise level of the PDs and the highest gain setting of the system, the dynamic range of the system (operating at 5 V) is approximately 74 dB.

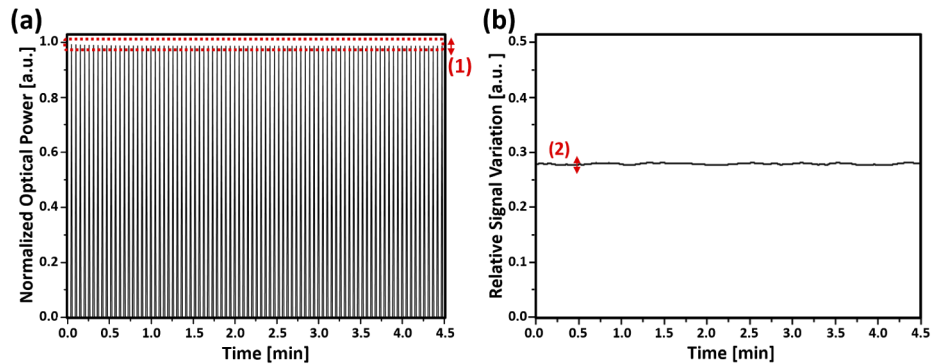


Fig. 5. System stability test of LEDs and PDs. (a) Fluctuation of optical power from LED pulse trains (1) RSD (Relative Standard Deviation) is 0.2%. (b) Variance of PD (1.7 mm^2 Si-PD) signal level with total gain of 320×10^3 , responding to the constant light intensity on the skin (2) RSD is 2.0%.

2.3. Measurement protocol

The proximal interphalangeal (PIP) joints were chosen because they are most often affected by lupus [40,41] and they have been evaluated in the previous studies [25]. For data acquisition from research subjects, a two-banded FOIS was wrapped around PIP joints of the index-, middle-, and ring-fingers and secured with medical tape (Micropore Surgical Tape, 3M). The first pair of source and detector [the one on the top-right corner in Fig. 6(a)] was always positioned on the bottom of finger as a reference point. The two bands included 8 of the integrated optical components consisting of 1 Si-PD and 3 LEDs (see Fig. 6). This set-up results in a total of $8 \times 3 \times 8 = 192$ source-detector pairs that surround the finger joint.

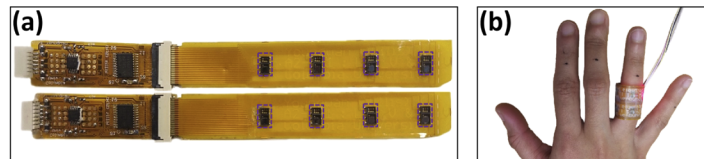


Fig. 6. Two FOISs and finger measurement (a) Two FOISs including 8 different locations (purple dotted line) of pair of 1 PD and 3 LEDs with wavelengths of 530 nm, 655 nm, and 940 nm. (b) Two FOISs wrapped around the 4th PIP joint.

The two-banded FOIS was used to measure the time-dependent light intensities transmitted through the finger during an inflated blood pressure cuff experiment. For our experiment, the cuff was placed around the forearm and inflated to 40 mmHg to elicit a hemodynamic response. The advantage of this approach is that the pre-stimulus state can be used as a reference or baseline against which the changes can be calibrated. As pointed out in several studies [25,42,43], these type of measurements allow the calculation of changes in oxy- and deoxyhemoglobin without the need for data calibration using a separate reference measurement, for example, on an Intralipid tissue phantom. This produced a partial venous occlusion. While the blood return was obstructed, arteries continued to supply blood to the hand. This leads to increase blood volume in the hand, which in turn leads to decreased light transmission. After cuff deflation, the blood drained from the hand and the optical transmission signals returned to pre-occlusion levels.

Optical data was acquired throughout the cuff experiment starting with a 60 seconds baseline measurement before the cuff was inflated. This was followed by a rapid inflation (< 3 seconds) to

40 mmHg, which was then held for another 60 seconds before the cuff was deflated. Measurements were continued for another 60 seconds to obtain a post-cuff baseline (Fig. 7).

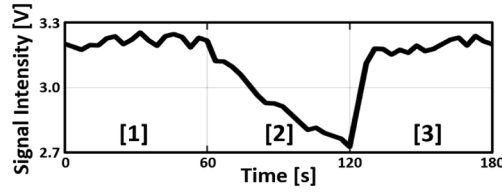


Fig. 7. Protocol of optical data acquisition for the cuff-experiment and each period [1] Baseline [2] Cuff-inflation [3] Post-cuff baseline.

2.4. Data processing

Once the raw data was recorded, it was processed for data analysis (See Fig. 8). The system obtains data at a frame rate of 0.5 Hz. At this rate the recorded signal may capture respiration effects (typically between 0.16 Hz and 0.33 Hz [44]) in addition to hemodynamics responses. We also observed some motion artifacts (e.g., short peaks around 20 seconds in Fig. 8). To filter out respiration and motion artifacts, we applied to all traces a discrete cosine transform (DCT) filter [13,45]. The following two formulas referred to as the DCT and the inverse DCT (iDCT) were employed:

$$\text{DCT} : X_k = \sum_{n=0}^{N-1} x_n \cos \left(\frac{k\pi}{N} \left(n + \frac{1}{2} \right) \right), k = 0, 1, 2, \dots, N - 1$$

$$\text{iDCT} : y_k = \frac{1}{2}x_0 + \sum_{n=1}^{N-1} X_k \cos \left(\frac{n\pi}{N} \left(k + \frac{1}{2} \right) \right), k = 0, 1, 2, \dots, K - 1$$

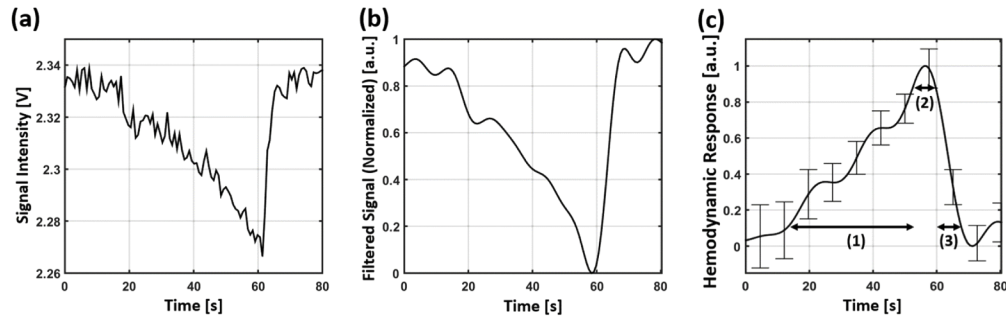


Fig. 8. Dynamic temporal responses to the cuff occlusion of 40 mmHg. (a) Raw signal intensity from one PD when one LED was on. (b) Normalized signal after DCT filtering process. (c) Normalized signal strength caused by hemodynamics processes extracted from the selected traces and three periods: (1) rise time t_r , (2) plateau time t_p , and (3) fall time t_f .

As can be seen, the DCT is a sum of cosine functions at different frequencies. It is similar to the discrete Fourier transform (DFT) but employs only real numbers [46–48]: Here x_n is the input data for n points recorded ($n = 60$) and N is the number of data acquired during the cuff-experiment (which in this case was 40). y_k is the filtered signal and K is the total number of DCT coefficients. Similar to the DFT, the more coefficients are used the higher the cut-off frequency [49,50]. Based on our previous experience in using the DCT [13,45] in optical imaging,

we used $K=15$ in this work. This removed noise components mentioned above, while maintaining the overall shape of traces.

Once all traces for all source-detector pairs were filtered, we normalized each trace using the following equation:

$$S_{Norm}(k) = \frac{y(k) - \text{Min}(y(k))}{\text{Max}(y(k)) - \text{Min}(y(k))}$$

In this way, $S_{Norm}(k)$ varies between zero and one (see Fig. 8(b)), and changes in the signal strength for each source-detector pair caused by the hemodynamic processes induced by the pressure cuff could be compared to each other.

Using the normalized traces, the overall hemodynamic response resulting from all source-detector pairs was considered. First, among a total of 192 ($8 \times 8 \times 3$) normalized traces, traces with an SNR below 10 dB were removed from the analysis. A mean trace extracted from all traces filtered and normalized was generated for each wavelength. The mean trace was reflected about x-axis and adjusted between 0 and 1 by the formula below:

$$y(k) = -\frac{\sum_{i=0}^n S_{Norm}(i)}{n} + 1$$

The resulting time-dependent signal [Fig. 8(c)] shows the hemodynamic effects induced by the venous cuff. The maximum value in Fig. 8(c) is the highest point of blood pooling at the location where the FOIS wrapped around the joint, while the pressure cuff was inflated. Therefore, this is the maximum time point of absorption by blood. For each wavelength, the standard deviation of the selected traces at a given time point were below ~ 0.3 .

For these time-traces, three parameters, called the rise time (t_r), the plateau time (t_p), and the fall time (t_f) were determined. The t_r is determined by measuring the time it takes for the signal to rise to 90% of the largest value starting from 10% of the largest value. The t_p is the time interval between points of 90% of the maximum from both the rising edge and falling edge. Finally, t_f is the time it takes for the signal to fall from 90% of the largest to 10% of the largest value at the backend of the response curve [See Fig. 8(c)].

2.5. Tomographic image reconstruction

The filtered time trace data was provided as input to the image reconstruction code that generates three-dimensional maps of hemodynamics (i.e., dynamic changes in total hemoglobin [tHb] concentration and tissue oxygenation [StO₂]) in the finger. We used a partial differential equation (PDE)-constrained reduced-space sequential quadratic programming (rSQP) method as used in our previous preclinical and clinical studies [13,16,25,51–54].

Starting with an estimate of the baseline hemoglobin concentration, the dynamic rSQP method reconstructs the time-varying 3D map of chromophores sequentially, sweeping through all subsequent time points by making use of the previous time point result as a new initial guess for the next time-point reconstruction.

The equation of radiative transfer (ERT) was used here as a light propagation model since the ERT is more accurate than the diffusion equation in describing light-tissue interactions in the media such as a finger that is of small volume and also contains the void-like region (i.e., synovial fluid in finger joints) [55]. We also used discrete cosine transformation (DCT) to compress tomographic images with a few DCT coefficients, which leads to a much efficient and better conditioned inverse problem where only a small number of DCT coefficients are to be found with the minimization procedure.

Three-dimensional volumetric PIP finger meshes were generated from surface meshes obtained with the laser scanner (DAVID Laser scanner), which was used right after the imaging session, as outlined in our previous work [16]. A typical 3D volume mesh was composed of approximately 42000 tetrahedron elements. Coregistration of optical components (i.e., sources and detectors)

on the 3D volume mesh were done based on the geometry of individual meshes (circumference of finger) and configuration of FOIS (distance between source-detector pairs, 15 mm) as described in Fig. 1(b). Each coordinate of optical components was calculated from the location of reference source-detector pair. Total hemoglobin concentrations were derived from consideration of all source/detector coupling together and initial concentrations were 20mM and 10mM for HbO₂ and Hb respectively.

3. Results

3.1. Hemodynamic trace analysis

To evaluate the potential of our two-banded FOIS for assessing SLE arthritis, we enrolled two patients with SLE (both females, age: 36 and 38) and two healthy volunteers (both females, age: 34 and 39). We examined each PIP joint of the index-, middle-, ring finger on both left and right hand. For 24 LEDs, a total of 192 (24 × 8) of signal traces were recorded per finger.

Figure 9 and 10 show three traces of hemodynamic responses at three different wavelengths [(a) $\lambda = 655$ nm, (b) $\lambda = 530$ nm, and (c) $\lambda = 940$ nm]. These traces were obtained from the raw signals (as described in the section 2.3), measured from three fingers of the two healthy volunteers (blue curves) and two patients with SLE arthritis (orange curves). We present the results as sets in order to highlight the differences between normal and lupus joints. The results focused on the period of cuff-inflation we are interested in.

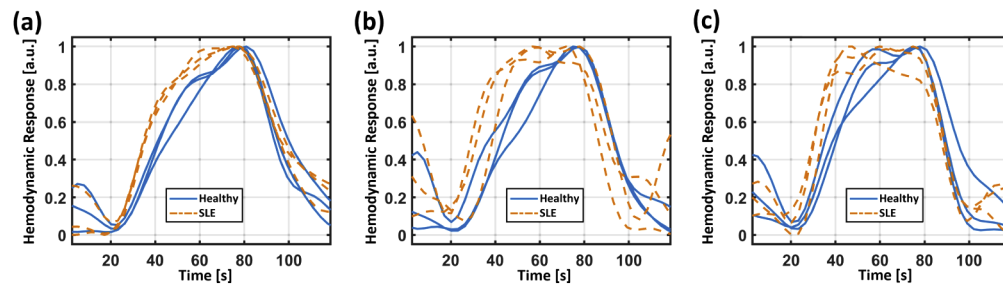


Fig. 9. Responses of local hemodynamics around the three different PIP joints of healthy control (blue solid line) and SLE patient (orange dashed line) responding to each wavelength 655 nm (a), 530 nm (b), and 940 nm (c) at the venous occlusion of 40 mmHg.

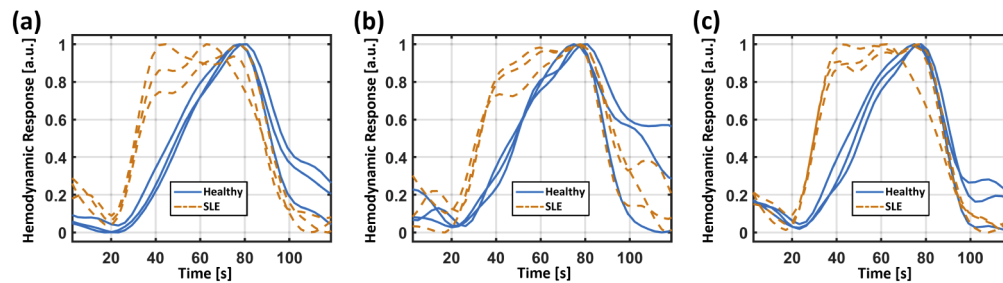


Fig. 10. Second set of hemodynamic responses (blue solid line: health control, orange dashed line: SLE patient) to the venous occlusion of 40 mmHg at the wavelengths of 655 nm (a), 530 nm (b), and 940 nm (c).

Looking at the data from the healthy volunteers (blue solid curves), one can observe a relatively slow increase in the absorption with the onset at ~ 20 seconds. This increase continues until the pressure cuff is released (at ~ 80 seconds). The increase is expected, as a 40 mmHg cuff induced

a venous occlusion, while the arteries are not affected. The arteries continue to deliver blood to the hand and fingers, the occluded veins prevent venous blood return. Consequently, blood is pooling in the finger, which leads to an increase of absorption at all wavelengths. When the cuff is released (at 80 seconds), the veins open again, and the blood can flow freely out of the fingers and hand, normal blood concentrations are restored. The absorption decreases to pre-occlusion levels.

The response in SLE fingers (orange dashed curves) to the 40 mmHg cuff is markedly different compared to the response in the healthy volunteers. The 90% point of the maximum absorption is reached much faster after inflating the cuff. Once 90% of the maximum absorption is reached it stays at that level until the cuff is released. The outflow is similar to the one observed in the healthy volunteer. As a result, we observed approximately two times shorter t_r and two times longer t_p in the SLE patients ($t_{r_MEAN} = 8.405$ [s], $t_{r_S.D.} = 2.308$ [s] and $t_{p_MEAN} = 8.853$ [s], $t_{p_S.D.} = 1.647$ [s]) compared with the healthy volunteers on average at all three wavelengths ($t_{r_MEAN} = 14.378$ [s], $t_{r_S.D.} = 0.698$ [s] and $t_{p_MEAN} = 4.413$ [s], $t_{p_S.D.} = 0.531$ [s]). The fall times t_f are about the same in the SLE patient and healthy volunteer ($t_{f_MEAN} = 8.321$ [s], $t_{f_S.D.} = 1.712$ [s]). We speculate that faster increase in light absorption, compared to normal joints, is caused by stiffer vessel walls in SLE patient. This would result in a smaller capacity of the vessels to expand and to increase the vascular volume [56,57]. Furthermore, inflammation of the tissue surrounding the joint is common in SLE patient. Inflammation is accompanied by an increase pooling of blood in the vasculature around the joint. An already increased blood concentration at the beginning of the measurement, would also limit the capacity to further increase the blood volume. Hence, 90% of the maximum light absorption is reached faster and maintained for a longer period of time as observed.

3.2. Analysis of tomographic data

In addition to the assessing the hemodynamic traces, we also used the hemodynamic data to generate 3-dimensional maps of total hemoglobin concentrations in these joints using the method described in section 2.5. For each finger of each subject a total of 40 volumetric maps (one every two seconds) were generated. Figure 11 shows a subset of these results for the same subjects described in Fig. 9.

Like Fig. 8(a), Fig. 11(a) shows an example of a raw signal that was obtained over the course of the cuff experiment, and which emphasizes the period of cuff-inflation and part of recovery period. The five green lines in Fig. 11(a) indicate the five different time points for which representative reconstructions are shown in Fig. 11(b) and 11(c). Here we chose one time point just before the cuff inflation (1), one time point in the middle of the inflation (2), one time point just before the release of the cuff (3), another point 20 seconds after the release of the cuff (4) and final time point 100-seconds after the release of the cuff, when the transmitted light signal reached a level comparable to the intensity at the beginning of the cuff experiment (5).

The top rows in Fig. 11(b) and 11(c), show 5 sagittal cross-sections of total hemoglobin (THb). The second and third rows show axial cuts at the tip side of finger and at the base side of finger, respectively. Two axial planes correspond to the positions where two FOIS were wrapped around. The bottom rows show coronal cuts. Figure 11(b) represents the results obtained from a healthy subject, while Fig. 11(c) shows results from a SLE patient.

Looking at the cross-sectional images of the finger of the healthy subject, one can observe an increase in THb in certain regions of the finger from the beginning of the cuff until the time point 3, when the pressure cuff is released. After the release, the THb reverts to pre-cuff levels. In general, this behavior is very similar to what we observed in the raw traces (see Fig. 9). However, while the raw traces only represent global hemodynamic behavior, averaged over the entire volume of the finger, these 3-dimensional images provide more spatial information about the location of these changes inside the finger [green-dotted boxes and blue-dotted boxes in

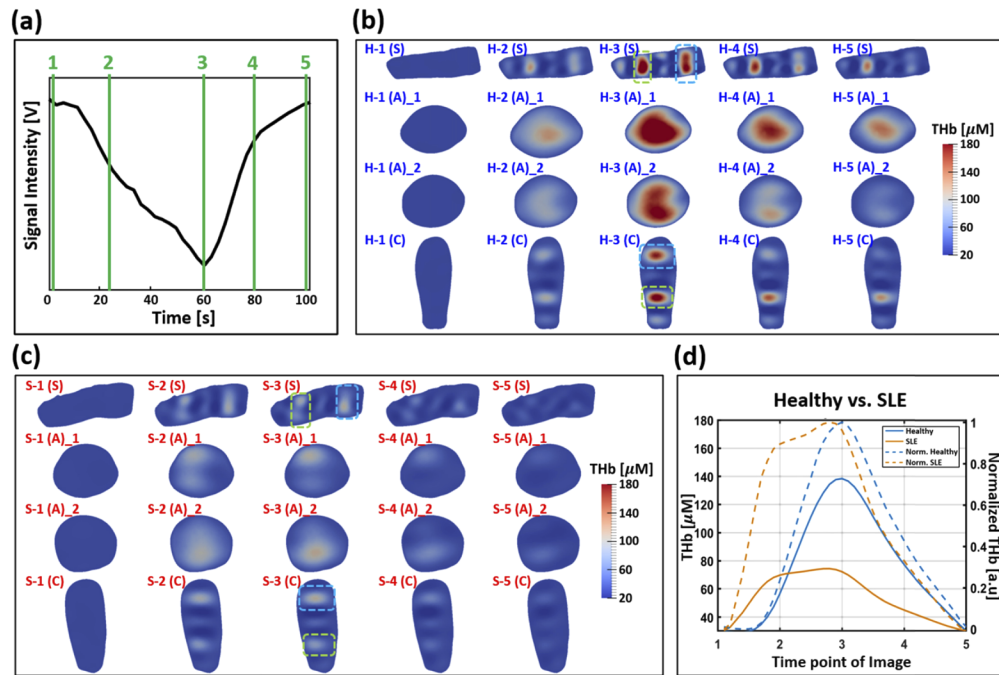


Fig. 11. Reconstructed results showing the concentration of total hemoglobin (THb): cross-sectional finger images based on anatomical planes (S: Sagittal, A: Axial, C: Coronal) at different time points. (a) Raw signal response to venous occlusion of 40 mmHg placed on forearm. The five green lines indicate the five different time points for which representative reconstructions are shown in (b) and (c) (1: baseline status, 2: inflating status, 3: peak inflation status, 4: deflating status, 5: rest status). Cross-sectional images of THb concentration from a healthy finger (b) and from a SLE finger (c). Cross-sectional images from the first row to the fourth row are sagittal images, axial images at a tip side of finger, axial images at a base side of finger, and coronal images. Two regions where two FOISs were wrapped around are shown as green-dotted box at the tip side of finger and blue-dotted box at the base side of finger. (d) Changes of average THb (straight line) at the given volume and normalized THb (dotted line) for each time point between a healthy (blue line) and a SLE finger (orange line).

Fig. 11(b) and 11(c). The closer a tissue volume is to the sources and detectors in the two FOIS bands, the higher the sensitivity is to the hemodynamic changes. This may be the reason that the biggest changes are observed in the volumes underneath these two rings. We expect that adding additional bands and tighter placing of source and detectors in future studies, will provide a higher spatial resolution over a larger volume of the finger.

To quantify the temporal responses observed in the tomographic data, we defined a region of interest (ROI) as area where the THb concentration is above 50% of the maximum value of THb concentration. Integrating over the values inside this ROI at each time point, results in a time trace seen in Fig. 11(d) (blue: healthy subject, orange: SLE patient). Compared to the results obtained with the healthy finger, THb values in images of the fingers of SLE patient are smaller. This would support the possibility of that the maximum blood pooling surround the joints can be easily reached due to inflammation in SLE patients. Applying the same ROI analysis as in the finger of the healthy control and SLE patient, we again derive a hemodynamic response curve. In addition to the amplitude difference, we also observe differences in the rise and plateau times, which we already observed when we performed the trace analysis in section 3.1. Furthermore, it appears that the fall time (or speed of outflow) is slower. This effect was

not visible from the hemodynamic trace analysis where it may have been averaged out. Very similar results were obtained from the second set of volunteers (see Fig. 12). Overall, the results show that our two-banded FOIS has the potential to distinguish healthy finger joints from joints affected by SLE.

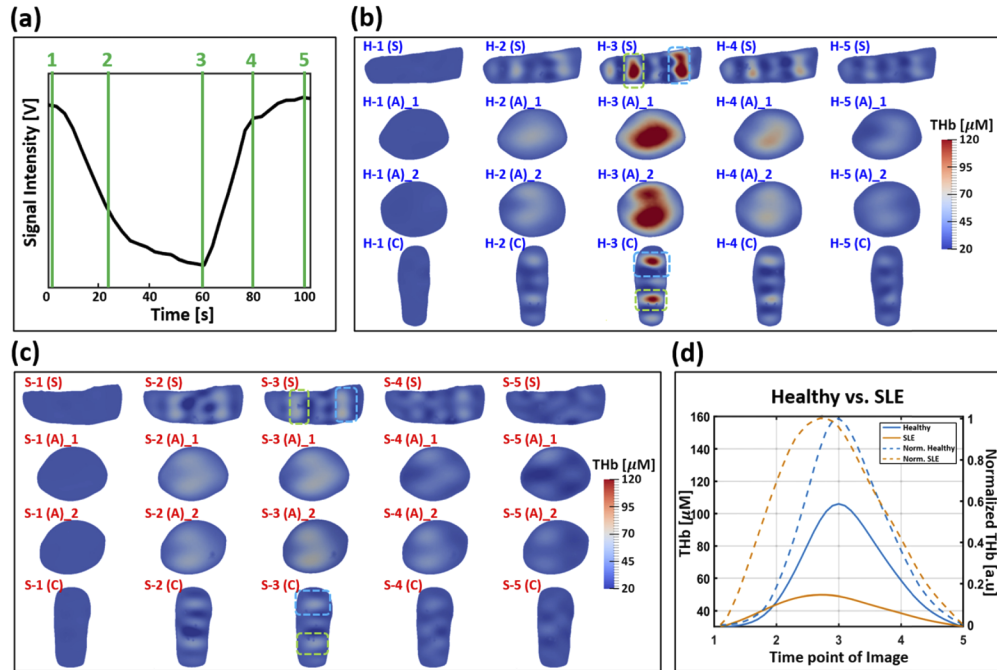


Fig. 12. The other set of reconstructed results for the five different time points indicated on raw signal (a) response to venous occlusion of 40 mmHg. The concentration of total hemoglobin (THb) of a healthy finger (b) and a SLE finger (c) are displayed on the basis of anatomical planes. At the given volume, straight lines and dotted lines show the changes of average THb and normalized THb respectively for a healthy finger (blue color) and a SLE finger (orange color) (d).

4. Summary and discussion

We have developed a low-cost, contrast-free, and easy-to-use system for the non-invasive evaluation of SLE arthritis. The total cost for the prototype system introduced in this study was below 100 dollars, which is substantially less than an ultrasound device (\$5,000 ~ \$100,000) or MRI system (> \$1,000,000). This modular flexible optical imaging system (FOIS) employs non-ionizing, near-infrared light and is composed of two key modules: a sensing band and a control band. The sensing band possesses four pairs of integrated optoelectronic components consisting of three LEDs and one PD. The control band consists of electronic components to access and read data from the sensing bands. The flexible form factor of FOIS provides conformal attachments to fingers, which have highly curved surfaces, resulting in a comfortable patient-interface. In this study, a FOIS consisting of two bands was used to measure the hemodynamic response to a venous cuff in two patients with SLE and two healthy volunteers. Three PIP joints (i.e., index-, middle-, ring-fingers) were examined for each of the 4 subjects. We found that in the SLE patient the rise time t_r in response to cuff pressure is shorter than in the healthy volunteer. On the other hand, the plateau time t_p in the SLE patient is longer than in the healthy subject.

Furthermore, 3-dimensional images were generated using an optical tomographic reconstruction algorithm. The tomographic images at the PIP finger joints of the healthy volunteers and SLE patients mapped the spatial distribution of total hemoglobin concentration. These images showed the changes of total hemoglobin concentration corresponding to the pressure cuff occlusion for each time point. In the regions of interest, a smaller change of THb was observed in the SLE patients compared to the change observed in healthy volunteers. The normalized THb was similar to the absorption profile in terms of hemodynamic response. We expect that in future studies, the use of more FOIS bands (e.g., one more band right over the PIP joint) can improve spatial resolution and even more accurately show changes in blood volume and oxygenation and their dependence on disease status. If confirmed in a study with a larger number of subjects, this technology would bring much needed objectivity to diagnosing and monitoring of SLE arthritis.

Funding. Fu Foundation School of Engineering and Applied Science (GT006737-03).

Acknowledgments. The authors thank the clinical research assistants, George Danias, Tommy K. Chen and Cathy A. Guo, for their help with patient consents, scheduling, and clinical evaluations. This work was supported in part by the Blavatnik Fund for Innovations in Health at the School of Engineering and Applied Science (SEAS) at Columbia University in the City of New York.

Disclosures. The authors declare that there are no conflicts of interest related to this article.

References

1. G. M. C. La Paglia, M. C. Leone, G. Lepri, R. Vagelli, E. Valentini, A. Alunno, and C. Tani, "One year in review 2017: systemic lupus erythematosus," *Clin Exp Rheumatol* **35**(4), 551–561 (2017).
2. T. Koutsokeras and T. Healy, "Systemic lupus erythematosus: lupus nephritis," *Nat. Rev. Drug Discov.* **13**(3), 173–174 (2014).
3. L. Lisnevskaja, G. Murphy, and D. Isenberg, "Systemic lupus erythematosus," *Brain Nerve* **384**, 1821–1900 (2014).
4. Q. Li, H. Wu, W. Liao, M. Zhao, V. Chan, L. Li, M. Zheng, G. Chen, J. Zhang, C. Lau, and Q. Lu, "A comprehensive review of immune-mediated dermatopathology in systemic lupus erythematosus," *J. Autoimmun.* **93**, 1–15 (2018).
5. J. E. Salmon and R. P. Kimberly, "Systemic Lupus Erythematosus," in *Hospital for Special Surgery Manual of Rheumatology and Outpatient Orthopedic Disorders: Diagnosis and Therapy*, 5th ed. (Lippincott Williams & Wilkins, 2006).
6. C. Tani, L. Carli, C. Stagnaro, E. Elefante, V. Signorini, F. Balestri, A. Delle Sedie, and M. Mosca, "Imaging of joints in systemic lupus erythematosus," *Clin. Exp. Rheumatol.* **36**(Suppl. 114), S68–S73 (2018).
7. C. L. Evans, "Peering inside the mind: Imaging brain activity with advanced diffuse optical tomography," *Sci. Transl. Med.* **8**(360), 360ec162 (2016).
8. M. A. Yücel, J. J. Selb, T. J. Huppert, M. A. Franceschini, and D. A. Boas, "Functional Near Infrared Spectroscopy: Enabling routine functional brain imaging," *Curr. Opin. Biomed. Eng.* **4**, 78–86 (2017).
9. D. A. Boas, A. M. Dale, and M. A. Franceschini, "Diffuse optical imaging of brain activation: Approaches to optimizing image sensitivity, resolution, and accuracy," *NeuroImage* **23**(Suppl. 1), S275–S288 (2004).
10. T. Durduran, R. Choe, W. B. Baker, and A. G. Yodh, "Diffuse optics for tissue monitoring and tomography," *Reports Prog. Phys.* **73**(7), 076701 (2010).
11. H. Sanada, Y. Higashi, C. Goto, K. Chayama, M. Yoshizumi, and T. Sueda, "Vascular function in patients with lower extremity peripheral arterial disease: A comparison of functions in upper and lower extremities," *Atherosclerosis* **178**(1), 179–185 (2005).
12. G. Di Leo, R. M. Trimboli, T. Sella, and F. Sardanelli, "Optical imaging of the breast: Basic principles and clinical applications," *Am. J. Roentgenol.* **209**(1), 230–238 (2017).
13. M. A. Khalil, H. K. Kim, I.-K. Kim, M. Flexman, R. Dayal, G. Shrikhande, and A. H. Hielscher, "Dynamic diffuse optical tomography imaging of peripheral arterial disease," *Biomed. Opt. Express* **3**(9), 2288 (2012).
14. J. W. Hoi, H. K. Kim, C. J. Fong, L. Zweck, and A. H. Hielscher, "Non-contact dynamic diffuse optical tomography imaging system for evaluating lower extremity vasculature," *Biomed. Opt. Express* **9**(11), 5597 (2018).
15. D. Chamberland, Y. Jiang, and X. Wang, "Optical imaging: New tools for arthritis," *Integr. Biol.* **2**(10), 496–509 (2010).
16. A. H. Hielscher, H. K. Kim, L. D. Montejo, S. Blaschke, U. J. Netz, P. A. Zwaka, G. Illing, G. A. Müller, and J. Beuthan, "Frequency-domain optical tomographic imaging of arthritic finger joints," *IEEE Trans. Med. Imaging* **30**(10), 1725–1736 (2011).
17. L. D. Montejo, J. Jia, H. K. Kim, U. J. Netz, S. Blaschke, G. A. Müller, and A. H. Hielscher, "Computer-aided diagnosis of rheumatoid arthritis with optical tomography, Part 1: feature extraction," *J. Biomed. Opt.* **18**(7), 076001 (2013).
18. L. D. Montejo, J. Jia, H. K. Kim, U. J. Netz, S. Blaschke, G. A. Müller, and A. H. Hielscher, "Computer-aided diagnosis of rheumatoid arthritis with optical tomography, Part 2: image classification," *J. Biomed. Opt.* **18**(7), 076002 (2013).

19. H. Y. Wu, A. Filer, I. Styles, and H. Dehghani, "Development of a multi-wavelength diffuse optical tomography system for early diagnosis of rheumatoid arthritis: simulation, phantoms and healthy human studies," *Biomed. Opt. Express* **7**(11), 4769 (2016).
20. D. Lighter, A. Filer, and H. Dehghani, "Multispectral diffuse optical tomography of finger joints," in *Diffuse Optical Spectroscopy and Imaging VI*, H. Dehghani, Ed., Vol. 10412 of *SPIE Proceedings (Optical Society of America, 2017)* (2017), p. 104120N.
21. D. Lighter, A. Filer, and H. Dehghani, "Detecting inflammation in rheumatoid arthritis using Fourier transform analysis of dorsal optical transmission images from a pilot study," *J. Biomed. Opt.* **24**(06), 1 (2019).
22. H. Dehghani, Y. Feng, D. Lighter, L. Zhang, and Y. Wang, "Deep neural networks improve diagnostic accuracy of rheumatoid arthritis using diffuse optical tomography," in *In Clinical and Preclinical Optical Diagnostics II, Vol. EB101 of SPIE Proceedings (Optical Society of America, 2019)* (2019), p. 11074_52.
23. Z. Yuan, Q. Zhang, E. Sobel, and H. Jiang, "Three-dimensional diffuse optical tomography of osteoarthritis: initial results in the finger joints," *J. Biomed. Opt.* **12**(3), 034001 (2007).
24. A. K. Scheel, A. Krause, I. Mesecke-Von Rheinbaben, G. Metzger, H. Rost, V. Tresp, P. Mayer, M. Reuss-Borst, and G. A. Müller, "Assessment of proximal finger joint inflammation in patients with rheumatoid arthritis, using a novel laser-based imaging technique," *Arthritis Rheum.* **46**(5), 1177–1184 (2002).
25. J. M. Lasker, C. J. Fong, D. T. Ginat, E. Dwyer, and A. H. Hielscher, "Dynamic optical imaging of vascular and metabolic reactivity in rheumatoid joints," *J. Biomed. Opt.* **12**(5), 052001 (2007).
26. A. Wunder, C. H. Tung, U. Müller-Ladner, R. Weissleder, and U. Mahmood, "In vivo imaging of protease activity in arthritis: A novel approach for monitoring treatment response," *Arthritis Rheum.* **50**(8), 2459–2465 (2004).
27. M. L. Flexman, H. K. Kim, R. Stoll, M. A. Khalil, C. J. Fong, and A. H. Hielscher, "A wireless handheld probe with spectrally constrained evolution strategies for diffuse optical imaging of tissue," *Rev. Sci. Instrum.* **83**(3), 033108 (2012).
28. N. Zhu, C.-Y. Huang, S. Mondal, S. Gao, C. Huang, V. Gruev, S. Achilefu, and R. Liang, "Compact wearable dual-mode imaging system for real-time fluorescence image-guided surgery," *J. Biomed. Opt.* **20**(9), 096010 (2015).
29. D. Chitnis, R. J. Cooper, L. Dempsey, S. Powell, S. Quaggia, D. Highton, C. Elwell, J. C. Hebden, and N. L. Everdell, "Functional imaging of the human brain using a modular, fibre-less, high-density diffuse optical tomography system," *Biomed. Opt. Express* **7**(10), 4275 (2016).
30. J. Kim, P. Gutruf, A. M. Chiarelli, S. Y. Heo, K. Cho, Z. Xie, A. Banks, S. Han, K.-I. Jang, J. W. Lee, K.-T. Lee, X. Feng, Y. Huang, M. Fabiani, G. Gratton, U. Paik, and J. A. Rogers, "Miniaturized battery-free wireless systems for wearable pulse oximetry," *Adv. Funct. Mater.* **27**(1), 1604373 (2017).
31. F. Teng, T. Cormier, A. Sauer-Budge, R. Chaudhury, V. Pera, R. Istfan, D. Chargin, S. Brookfield, N. Y. Ko, and D. M. Roblyer, "Wearable near-infrared optical probe for continuous monitoring during breast cancer neoadjuvant chemotherapy infusions," *J. Biomed. Opt.* **22**(1), 014001 (2017).
32. L. Di Sieno, J. Nissinen, L. Hallman, E. Martinenghi, D. Contini, A. Pifferi, J. Kostamovaara, and A. D. Mora, "Miniaturized pulsed laser source for time-domain diffuse optics routes to wearable devices," *J. Biomed. Opt.* **22**(08), 1 (2017).
33. Y. Tomioka, S. Enomoto, J. Gu, A. Kaneko, I. Saito, Y. Inoue, T. Woo, I. Koshima, K. Yoshimura, T. Someya, and M. Sekino, "Multipoint tissue circulation monitoring with a flexible optical probe," *Sci. Rep.* **7**(1), 1–13 (2017).
34. M. J. Saikia, W. G. Besio, and K. Mankodiya, "WearLight: toward a wearable, configurable functional nir spectroscopy system for noninvasive neuroimaging," *IEEE Trans. Biomed. Circuits Syst.* **13**(1), 1 (2018).
35. M. Lacerenza, M. Buttava, M. Renna, A. Dalla Mora, L. Spinelli, F. Zappa, A. Pifferi, A. Torricelli, A. Tosi, and D. Contini, "Wearable and wireless time-domain near-infrared spectroscopy system for brain and muscle hemodynamic monitoring," *Biomed. Opt. Express* **11**(10), 5934–5949 (2020).
36. R. Istfan, D. M. Roblyer, S. Larochelle, and R. Chaudhury, "A miniature frequency domain diffuse optical optode for quantitative wearable oximetry," *Proc. SPIE* **10874**, 108742B (2019).
37. M. K. Ghosh and K. L. Mittal, *Polyimides: Fundamentals and Applications* (Marcel Dekker Inc, 1996).
38. Y. Kim, A. Marone, G. Danias, K. E. Neville, A. T. Frantz, T. Kapoor, L. Geraldino-Pardilla, I. Kymissis, A. D. Askanase, A. H. Hielscher, and H. K. Kim, "Flexible electronic bands for the dynamic optical spectroscopic assessment of systemic lupus erythematosus in finger joints," *Proc. SPIE* **108850**, 108850Z (2019).
39. E. F. Schubert, *Light-Emitting Diodes* (Cambridge University Press, 2003).
40. F. Tamirou, L. Arnaud, R. Talarico, C. A. Scirè, T. Alexander, Z. Amoura, T. Avcin, A. Bortoluzzi, R. Cervera, F. Conti, A. Cornet, H. Devilliers, A. Doria, M. Frassi, M. Fredi, M. Govoni, F. Houssiau, A. Lladò, C. Macieira, T. Martin, L. Massaro, M. F. Moraes-Fontes, C. Pamfil, S. Paolino, C. Tani, S. W. Tas, M. Tektonidou, A. Tincani, R. F. Van Vollenhoven, S. Bombardieri, G. Burmester, F. J. Eurico, I. Galetti, E. Hachulla, U. Mueller-Ladner, M. Schneider, V. Smith, M. Cutolo, M. Mosca, and N. Costedoat-Chalumeau, "Systemic lupus erythematosus: State of the art on clinical practice guidelines," *RMD Open* **4**(Suppl. 1), 1–6 (2019).
41. M. Olesińska and A. Saletra, "Quality of life in systemic lupus erythematosus and its measurement," *Reumatologia* **56**(1), 45–54 (2018).
42. A. H. Hielscher, A. D. Klose, A. K. Scheel, B. Moa-Anderson, M. Backhaus, U. Netz, and J. Beuthan, "Sagittal laser optical tomography for imaging of rheumatoid finger joints," *Phys. Med. Biol.* **49**(7), 1147–1163 (2004).
43. D. Golovko, R. Meier, E. Rummeny, and H. Daldrop-Link, "Optical imaging of rheumatoid arthritis," *Int. J. Clin. Rheumatol.* **6**(1), 67–75 (2011).

44. M. A. Russo, D. M. Santarelli, and D. O'Rourke, "The physiological effects of slow breathing in the healthy human," *Breathe* **13**(4), 298–309 (2017).
45. X. Gu, K. Ren, J. Masciotti, and A. H. Hielscher, "Parametric image reconstruction using the discrete cosine transform for optical tomography," *J. Biomed. Opt.* **14**(6), 064003 (2009).
46. N. Ahmed, T. Natarajan, and K. R. Rao, "Discrete cosine transform," *IEEE Trans Comput* **C-23**(1), 90–93 (1974).
47. A. K. Jain, *Fundamentals of Digital Image Processing* (Prentice-Hall, 1989).
48. W. B. Pennebaker and J. L. Mitchell, *JPEG: Still Image Data Compression Standard* (Van Nostrand-Reinhold, 1993).
49. E. B. Lum, K. L. Ma, and J. Clyne, "Texture hardware assisted rendering of time-varying volume data," Proc. IEEE Vis. Conf. D, 263–270 (2001).
50. S. Lian, J. Sun, and Z. Wang, "A novel image encryption scheme based-on JPEG encoding," *Proc. Int. Conf. Inf. Vis.* **8**, 217–220 (2004).
51. H. K. Kim, M. Flexman, D. J. Yamashiro, J. J. Kandel, and A. H. Hielscher, "PDE-constrained multispectral imaging of tissue chromophores with the equation of radiative transfer," *Biomed. Opt. Express* **1**(3), 812 (2010).
52. H. K. Kim and A. H. Hielscher, "A PDE-constrained SQP algorithm for optical tomography based on the frequency-domain equation of radiative transfer," *Inverse Probl.* **25**(1), 015010 (2009).
53. A. H. Hielscher, A. Klose, and J. Beuthan, "Evolution strategies for optical tomographic characterization of homogeneous media," *Opt. Express* **7**(13), 507–518 (2000).
54. M. L. Flexman, M. A. Khalil, R. Al Abdi, H. K. Kim, C. J. Fong, E. Desperito, D. L. Hershman, R. L. Barbour, and A. H. Hielscher, "Digital optical tomography system for dynamic breast imaging," *J. Biomed. Opt.* **16**(7), 076014 (2011).
55. A. H. Hielscher, R. E. Alcouffe, and R. L. Barbour, "Comparison of finite-difference transport and diffusion calculations for photon migration in homogeneous and heterogeneous tissues," *Phys. Med. Biol.* **43**(5), 1285–1302 (1998).
56. H. Raff, *Physiology Secrets*, 2nd ed. (Elsevier Health Sciences, 2003).
57. C. V. Ioannou, N. Stergiopoulos, A. N. Katsamouris, I. Startchik, A. Kalangos, M. J. Licker, N. Westerhof, and D. R. Morel, "Hemodynamics induced after acute reduction of proximal thoracic aorta compliance," *Eur. J. Vasc. Endovasc. Surg.* **26**(2), 195–204 (2003).